This article has been accepted for publication in a future issue of this journal, but has not been fully edited. Content may change prior to final publication. Citation information: DOI 10.1109/JPHOT.2020.3012097, IEEE Photonics Journal

Automated Adaptation and Stabilization of a Tunable WDM Polarization-Independent Receiver on Active Silicon Photonic Platform

Minglei Ma, Hossam Shoman, *Student Member, IEEE*, Sudip Shekhar, *Senior Member, IEEE*, Nicolas A. F. Jaeger, *Member, IEEE*, and Lukas Chrostowski, *Senior Member, IEEE*

Department of Electrical and Computer Engineering, University of British Columbia, Vancouver, B.C., V6T 1Z4, Canada

DOI: 10.1109/JPHOT.2009.XXXXXXX

Manuscript received XXX, 2020; revised XXX, 2020. This research was funded by Natural Sciences and Engineering Research Council (NSERC) of Canada, particularly the Silicon Electronic-Photonic Integrated Circuits (SiEPIC) Program. Minglei Ma and Hossam Shoman equally contribute to this work. Corresponding author: Minglei Ma (e-mail: mingleim@ece.ubc.ca).

Abstract: We demonstrate automated adaptation and stabilization of a silicon photonic wavelength-division multiplexing (WDM), polarization-independent receiver. A two-channel, tunable WDM polarization-independent receiver is designed and used to demonstrate automated WDM polarization control. Using a control algorithm based on Barzilai and Borwein's two-point step size gradient descent method, we realize automated polarization adaptation and wavelength stabilization for two arbitrarily polarized input data streams. 10 Gb/s on-off keying and 20 Gb/s pulse-amplitude modulation 4-level formats are generated as the high-speed input data streams. In addition, we implement a long-duration experiment, in which we measure the bit-error-ratio for continuously varying polarization states and changing chip temperatures. The experimental results show that, with the automated control, the WDM polarization-independent receiver can adapt, stabilize, and track the arbitrary input polarization states from a standard optical fiber into the transverse electric mode of a silicon waveguide and simultaneously stabilize the transmitted wavelength channels at various chip temperatures. We also show how the presented WDM polarization-independent receiver scales with N channels and propose an improved design for large-scale WDM applications.

Index Terms: Photonic integrated circuits, automatic control, silicon photonics, optical polarization, wavelength division multiplexing, demultiplexing.

1. Introduction

Photonic integrated circuits (PICs) can realize high-speed optical communication and computing through the dense-integration of high-performance devices with minimal form factors [1], [2]. Specifically, silicon PICs are compatibile with CMOS fabrication processes, which enables large-scale integration at low-cost. For efficient transmission, techniques such as wavelength-division multiplexing (WDM) is used to increase the data handling capacity in a single optical fiber link. This, however, requires a receiver that can resolve the wavelength at which each data stream is transmitted. In addition, since low-cost, commercial optical fibers are not polarization maintaining (PM), on-chip receivers should also be able to adapt the polarization state of each input wavelength channel. Polarization transparent schemes are typically realized using polarization dependent

This article has been accepted for publication in a future issue of this journal, but has not been fully edited. Content may change prior to final publication. Citation information: DOI 10.1109/JPHOT.2020.3012097, IEEE Photonics Journal

components (mostly designed for TE mode operation) [3]–[5]. For example, a polarization diversity circuit is a subsystem that splits the input light into two branches using a polarization beam splitter (PBS), polarization splitting grating coupler (PSGC), or a polarization splitter-rotator (PSR), and implements two identical circuits, one for each branch. Over the last decade, this method has been intensively used and reported to develop various on-chip WDM receivers [6]–[13]. Such designs generally need to have two identical copies of data processing circuits for each wavelength channel, as shown in Fig. 1(a). Alternatively, an active, on-chip polarization controller [14]–[17]

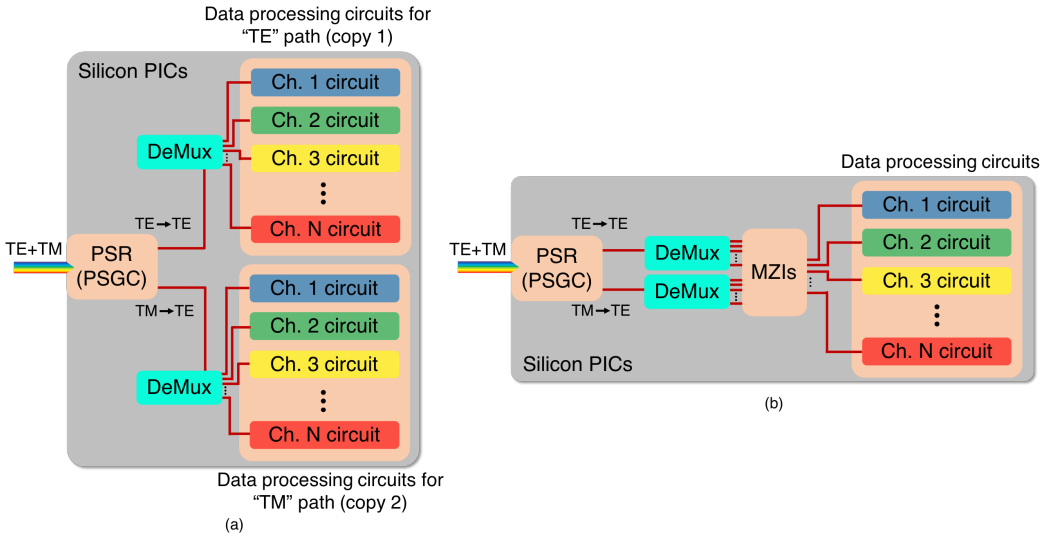

Fig. 1. WDM polarization control for N channel data processing circuits. (a) A polarization diversity scheme using a PSR (PSGC) and two demultiplexers (DeMuxes). (b) A WDM, active polarization control scheme using a PSR (PSGC), two demultiplexers (DeMuxes), and N tunable MZIs.

uses a tunable Mach-Zehnder interferometer (MZI) to actively manage the input polarization of each channel and passes the optimized output light to the data processing circuits. This approach can enable the automated on-chip polarization control [18] and also save the cost of duplicating the circuits, especially for complex or large scale circuits that may need many electrical controls [19]–[26], as shown in Fig. 1(b). Therefore, implementing on-chip WDM polarization control based on the above schemes is a promising and essential approach to realize real-estate-efficient, fully-monolithic systems designed to process data for multiple wavelength channels simultaneously.

In this paper, we experimentally demonstrate the automated adaptation and stabilization of a silicon photonic WDM polarization-independent receiver (WDM PR). A two-channel, tunable WDM PR was designed and used to demonstrate the automated wavelength and polarization control. Due to the ability to simultaneously sense (by measuring the photocurrent) and control (via the applied voltage) their resonance condition, compact micro-ring resonators (MRRs) with in-resonator photoconductive heaters (IRPHs) [27] are used for the wavelength filters in our WDM PR. The outputs of the MRR filters with IRPHs are then combined by the tunable MZI, which removes the need to duplicate the signal processing circuit. Therefore, using MRRs with IRPHs and tunable MZIs enables us to automatically adapt, and simultaneously stabilize any arbitrary input polarization state into the TE mode of the output waveguide for each wavelength channel. Also, a control algorithm based on Barzilai and Borwein's two-point step size gradient descent method (B-B GD) [18], [28] is used to realize the automated wavelength and polarization control. By generating arbitrarily polarized, modulated data streams (on-off keying (OOK) and pulse-amplitude modulation 4-level (PAM-4)) in a standard optical fiber, we implement the automated polarization and wavelength adaptation in our WDM PR. To assess the practicality of our approach, the stabilization capabilities of the automated control for both wavelength channels are also

This article has been accepted for publication in a future issue of this journal, but has not been fully edited. Content may change prior to final publication. Citation information: DOI 10.1109/JPHOT.2020.3012097, IEEE Photonics Journal

evaluated over a long period of time in which the input polarization states and the chip temperature of our WDM PR are continuously changed.

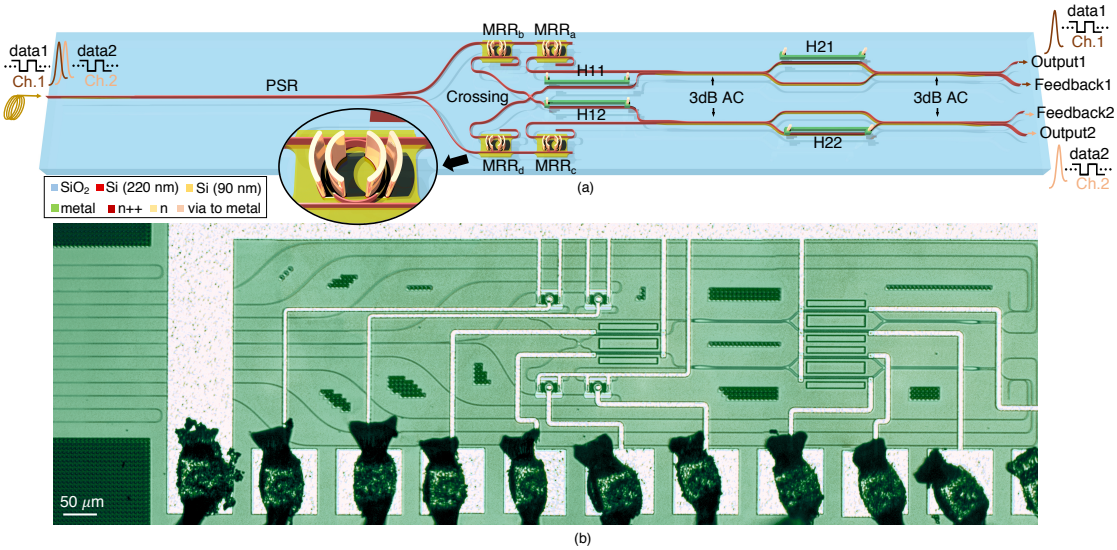

Fig. 2. (a) Schematic of the two-channel WDM PR for two wavelength channels each having arbitrarily polarized inputs (SiO_2 cladding layer is not included in this figure). Inset figure: Zoom-in of an MRR filter with an IRPH. (b) An optical micrograph of a fully fabricated two-channel WDM PR.

2. Two-channel WDM PR design and control principle

Fig. 2 (a) shows a schematic of our two wavelength channel WDM PR. The proposed system consists of a broadband PSR [14], four tunable MRRs with IRPHs, an optical crossing [29], and two tunable MZIs that include broadband 3 dB adiabatic couplers (ACs) [30]. The MRRs have radii of 10 μm and symmetric bus-ring coupling gaps of 200 nm, for bus-ring power coupling strengths of $\sim$ 11%, and the IRPHs occupied two-thirds of the MRRs' circumferences. The measured 3 dB bandwidths were $\sim$ 42 GHz, which was more than sufficient to demonstrate the recovery of 10 Gb/s modulated signals. Each of the components used has a low insertion loss of less than 0.5 dB; less than 0.2 dB for the PSR, less than 0.4 dB for an MRR with an IRPH, less than 0.5 dB for an optical crossing, and less than 0.2 dB for an AC. We choose broadband nano-tapers [4] as the optical interfaces between the optical fibers and our on-chip system. For both of the wavelength channels, the TE insertion loss (including the edge-coupling losses) was estimated $\sim$ 6.2 dB and the TM insertion loss (also including the edge-coupling losses) was estimated to be $\sim$ 7.4 dB. The input light, in the two channels, each having an arbitrary polarization state, is predominately coupled into the TE_{00} and TM_{00} modes in the nano-taper and propagates into the PSR. The adiabatic PSR evolves these TE_{00} and TM_{00} modes into the TE_{00} modes of its two single-mode output waveguides, and then transmits these TE_{00} output modes to the MRR filters (MRR_a to MRR_d in Fig. 2(a)). By configuring the voltages applied to the IRPHs (Inset in Fig. 2(a)), the MRRs can be tuned to separate the two channels, for each of the PSR outputs, and guide them to the MRRs' drop-ports. Following the MRR filters, the outputs for one channel (Ch. 1) are guided to the upper MZI, and the outputs for the other channel (Ch. 2) are guided to the lower MZI; to accomplish this, a broadband optical crossing is used in one of the optical paths for each channel. Then, by tuning the thermal phase shifters (H11, H21, H12, and H22 in Fig. 2(a)), the optical power at the feedback port of each MZI is minimized so that the optical power at its output port is maximized. In this way, an arbitrary input polarization state from the optical fiber can be adapted to the TE_{00} mode of the output waveguide for each wavelength channel. A control

algorithm is employed [18] to realize automated adaptation and stabilization for both wavelength and polarization.

Here, we will present a concise description of the automated control algorithm; detailed discussions can be found in [18]. To realize automated control, for both wavelength and polarization, we use a mathematical minimum/maximum optimization method - B-B GD method [28]. Fig. 3 is a flow diagram of the control algorithm. The variable vector $\boldsymbol{x}_i$ corresponds to the voltages applied to the IRPHs in the MRR filters or the currents passed through thermal phase shifters. Similarly, the gradient $\boldsymbol{g}_i$ is correlated to the photocurrents of the IRPHs or the optical feedback power of the WDM-PR. The step size of the variable vector is related to a term $\pm\ \alpha_i \cdot \boldsymbol{g}_i$, where α_i is a scalar factor for each iteration and it is determined by the following equation:

$$\alpha_i = \Delta\boldsymbol{x}_i \cdot \Delta\boldsymbol{g}_i^T / \|\Delta\boldsymbol{g}_i\|^2 \tag{1}$$

In Eq. 1, $\Delta\boldsymbol{x}_i = \boldsymbol{x}_i - \boldsymbol{x}_{i-1}$, $\Delta\boldsymbol{g}_i = \boldsymbol{g}_i - \boldsymbol{g}_{i-1}$, and this indicates the step size, $\pm\ \alpha_i \cdot \boldsymbol{g}_i$, depends on the adjacent points in each iteration. A threshold number σ is given to end the control loop when the norm of $\boldsymbol{g}_i$ decreases to the convergence level. Therefore, by automatically controlling the voltages applied to the IRPHs and the currents passing through the thermal phase shifters using this B-B GD based control method, we can continuously track and stabilize the maximum photocurrent in the IRPHs of our MRR filters and the minimum power at the feedback port of our WDM PR, respectively. Here, it should be noted that the automated control algorithm that stabilizes the MRR filters will reach a “halt” when the photocurrent read by an IRPH drops below a specified “low” level threshold, that can occur due to the changing input polarization state, and the algorithm will continue when the IRPH’s photocurrent again rises above the low level threshold (e.g., 10% of the maximum photocurrent). Therefore, halting can result in small input power penalties that depend on the chosen threshold. It is worth mentioning that the IRPHs used has a resolution of 1.5 μW [24] and, thus, the power penalty is expected to be low.

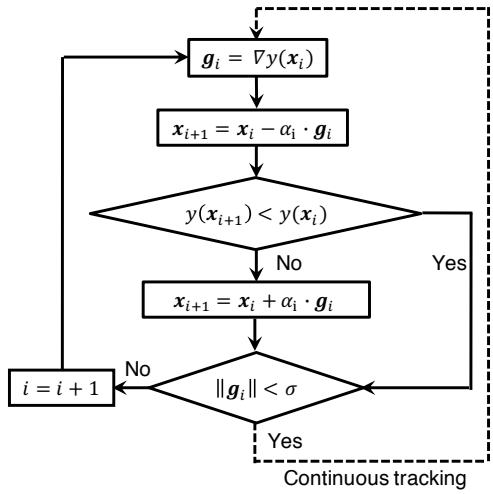

Fig. 3. A flow diagram illustrating B-B GD-based minimization method for the control algorithm.

3. Experimental Details

The test structures were fabricated using 193 nm optical lithography at the Institute of Microelectronics (IME), Singapore. An optical micrograph of a fabricated two-channel WDM PR is shown in Fig. 2 (b). Low resistance aluminum wire-bonds are used to connect the on-chip bond-pads to the electrical power sources for tuning the MRRs’ IRPHs and the MZIs’ thermal phase shifters. We chose two neighbouring ITU wavelength channels, 1554.13 nm (Ch. 1) and 1555.75 nm (Ch. 2) on

a 200 GHz grid, as the WDM input signals. Therefore, by locating the voltages that maximize the photocurrents measured by the MRRs' IRPHs, the desired wavelength channels can be obtained at the drop-ports of the corresponding MRR filters. As an example, Fig. 4 shows the as-fabricated and tuned spectra of an MRR's calibration structure, and the locating voltages (V_1 to V_2) applied to the IRPHs for both chosen wavelength channels.

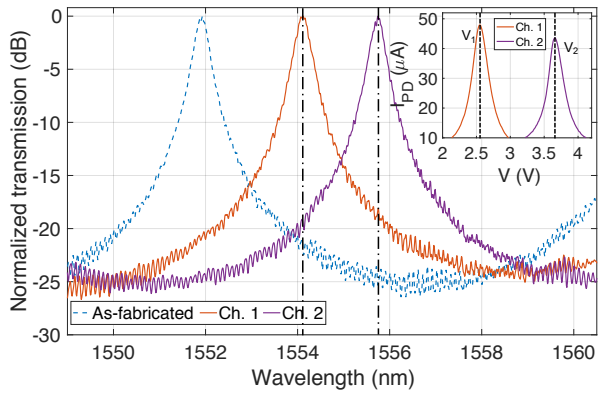

Fig. 4. Normalized drop-port spectra as-fabricated and after tuning an MRR first to Ch. 1 and then to Ch. 2. Inset Fig.: Photocurrent I_{PD} measured in the MRR's IRPH while tuning to Ch. 1 and to Ch. 2. Applied voltages V_1 and V_2 are found when locating the maximum photocurrent of the IRPH to Ch. 1 and to Ch. 2, respectively.

A high-speed experimental setup was built to characterize the automated adaptation and stabilization for the tested WDM PR, as shown in Fig. 5. Two optical light sources (Laser 1 and Laser 2) are provided by a Keysight N7714A multi-channel laser source. Then, two non-return-to-zero (NRZ) $2^{31}-1$ pseudorandom binary sequence (PRBS) data streams, generated by two pulse pattern generators, an Anritsu MU183020A (PPG1) and an Anritsu MP1763B (PPG2), were applied to two $LiNbO_3$ Mach-Zehnder modulators (MZM1 and MZM2) to generate the data stream for each wavelength channel. In one channel path, an HP 11896A polarization controller (PC) was used to generate the arbitrary polarization states, and, a 10/90 PM fiber-optic tap was used to couple 10 percent of the transmission into an HP 8509B polarization analyzer (PA), which can give the locations of the input polarization state on the Poincaré sphere. We calibrated the PA using s and p polarized input light. Other than the fiber in the PC, all of the fibers used throughout our test setup were PM fibers. Here, it should be mentioned that, for arbitrary polarization states recorded by the PA, the ratios of the s and p polarizations and their phase differences determine the points on the Poincaré sphere. Hence, by using a PM fiber tap together with the PA, we can know relative amounts of s and p polarizations, but we cannot know their phase differences at the input to the chip. Nevertheless, the arbitrary polarization states recorded on the Poincaré sphere provide evidence that a range of polarization states were injected into our on-chip system [18]. Then, the two wavelength channel inputs, each having identical optical power, were combined using a PM 3 dB fiber-optic coupler. An SRS LDC501 thermoelectric cooler (TEC) was used to manage the temperature of the tested chip. For the on-chip active control process, Keithley 2604B source-measure units (SMUs) and an HP 81635A optical power sensor (PD) were used to tune the thermal phase shifters and read the optical power at the feedback port of our WDM PR, respectively. The output optical signal was then detected using an HP 11982 high-speed lightwave converter (Rx), and an erbium-doped fiber amplifier (EDFA) and a variable optical attenuator (VOA) were placed ahead of the Rx to set a desired optical power level. Finally, the detected RF output was sent to an Agilent 86100A sampling oscilloscope with a HP 83484A 50 GHz sampling head for the eye diagram measurements and an Anritsu MU183040B error detector (ED) for the bit-error ratio (BER) measurements.

Figs. 6(a)-(d) show a 10 Gb/s OOK data stream at Ch. 1 measured at various stages of the

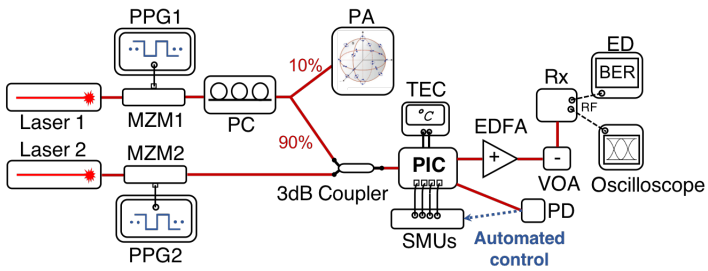

Fig. 5. Schematic of the experimental setup for eye diagram and BER measurements.

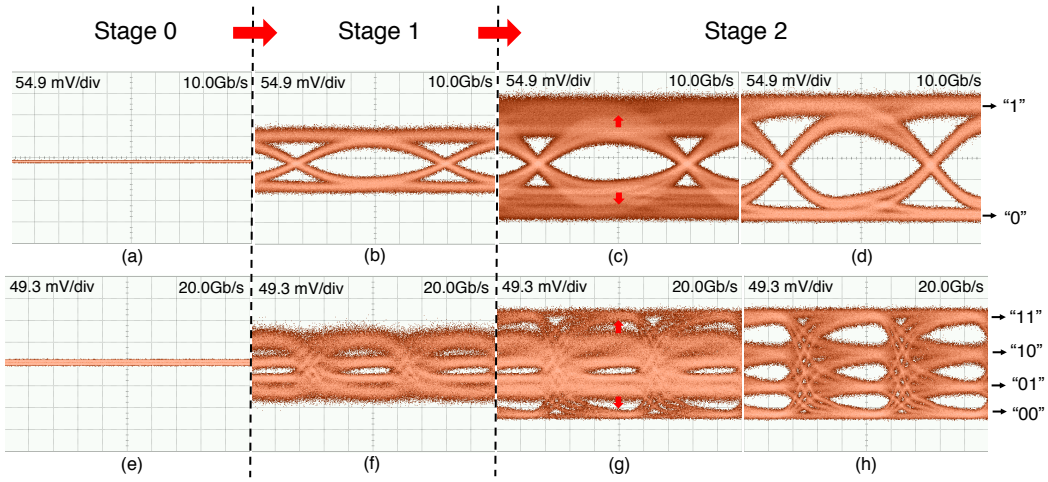

Fig. 6. Recorded eye diagrams for Ch. 1, (a) - (d) OOK and (e) - (h) PAM-4 output signal at each control stage: In Stage 0, (a), (e), all of control was offline; In Stage 1, (b), (f), the desired channel (Ch. 1) was found by configuring MRR's IRPH; In Stage 2, eye opening (c), (g) during and (d), (h) after the automated polarization adaptation.

automated control process when a second 10 Gb/s OOK data stream was present at Ch. 2. Similarly, Figs. 6(e)-(h) show a 20 Gb/s PAM-4 data stream (generated using two synchronized, PPGs and combined using a Wilkinson's combiner [31]) at Ch. 1 at various stages of the automated control process when a 10 Gb/s OOK data stream was transmitted at Ch. 2. In Stage 0, as shown in Figs. 6(a) and 6(e), since the active controls were offline and the input channels did not match the as-fabricated resonances of the MRR filters, closed eyes for Ch. 1 were recorded. In Stage 1, the applied voltages for the corresponding MRRs' IRPHs (MRR_a and MRR_d in Fig. 2(a)), were varied to maximize the measured photocurrent in each MRR. The photocurrent was obtained by subtracting the IRPH's current when the laser was on from the IRPH's current when the laser was off (dark current) [24]. Thus, we obtained a photocurrent signal that is maximized when the ring's resonance is aligned to the laser's frequency. This led to the output signal having a relatively open eye, i.e., a ∼71.5 mV eye height (from level "0" to level "1") for OOK transmission and eye heights of ∼0 mV, ∼17.9 mV, and ∼12.2 mV (from level "00" to level "11") for PAM-4 transmission, see Figs. 6(b) and 6(f). After the wavelength channel tuning, i.e., in Stage 2 as shown in Figs. 6(c) and 6(d), and in Figs. 6(g) and 6(h), by using the B-B GD method-based control algorithm, the MZI's thermal phase shifters (H11 and H21 in Fig. 2(a)) were automatically tuned so that the optical power at the feedback port was minimized and increased eye-openings were observed at the output port, where a ∼166.9 mV eye height (from level "0" to level "1") for OOK transmission and eye heights of ∼35.9 mV, ∼39.7 mV, and ∼46.1 mV (from level "00" to level

This article has been accepted for publication in a future issue of this journal, but has not been fully edited. Content may change prior to final publication. Citation information: DOI 10.1109/JPHOT.2020.3012097, IEEE Photonics Journal

"11") for PAM-4 transmission were obtained. Hence, our WDM PR achieved automated wavelength and polarization control for Ch. 1. Here, it should be noted that the thermal fluctuations of the on-chip system, such as environmental temperature variations, and thermal crosstalk introduced by the thermal phase shifters, will lead to a resonant wavelength-drift in the MRRs which, in turn, may cause the eyes close at the output. Hence, automated stabilization of the configured MRRs' IRPHs was implemented for our WDM PR.

Therefore, we implemented a long-duration adaptation and stabilization experiment in which we continuously varied the input polarization states and the chip temperature. The two wavelength channel input signals, each having equal optical power and separate data streams (10 Gb/s OOK), were simultaneously transmitted into the chip. Here, we passed one channel through the PC at a time and recorded the effects of polarization and temperature change for that channel. The other channel's polarization was free to drift, but was not forced to change (it was, however, subjected to the same temperature change). The experimental results for these two channels, i.e., Ch. 1 and Ch. 2, are shown in Fig. 7. As we mentioned previously, s and p polarized light was used to calibrate the PA. Then, using the external PC, we generated arbitrary polarization states to inject into our WDM PR. In Fig. 7(a), the points measured by the PA, and given by normalized Stokes parameters (S1, S2, and S3 plotted on the right-hand side of Fig. 7(a)), provide the various polarization states for Ch. 1 and Ch. 2. Simultaneously, we varied the chip temperature by controlling the TEC. In our test, the chip temperature was set to increase linearly from $\sim$26 °C to $\sim$33 °C as shown in Fig. 7(b). Thus, as discussed earlier, to tackle the wavelength-drift in the tuned MRRs, i.e., stabilize the IRPHs' maximized photocurrents, the voltages applied to the IRPHs were automatically adjusted using the B-B GD-based control algorithm [18]. In this way, as shown in Fig. 7(d), when the chip temperature was increased, i.e., the MRRs' resonances were red-shifted, the tuning voltages applied to the MRRs' IRPHs (MRR_a - MRR_d) were decreased, (i.e., to compensate for the red-shift) during the automated control process. Hence, with constantly stabilized MRR filters, we could implement the automated adaptation and stabilization for two arbitrarily polarized inputs. As shown in Fig. 7(c), we can see that, for both wavelength channels, the optical powers at the feedback port were constantly minimized and stabilized at a $>$30 dB power extinction ratio (relative to the power at the output port) and this led to the measured BERs staying at lower levels ($10^{-9}\sim10^{-10}$). Here, it should be noted that the fluctuations of the optimized BER data mainly resulted from minor changes in the optical coupling. Additionally, we also recorded the various electric powers applied to the MZIs' thermal phase shifters (H11, H21 for Ch. 1, and H12, H22 for Ch. 2 in Fig. 7(e)). These tracks reflect the automated adaptation and stabilization process, which corresponds to the output responses as shown in Fig. 7(c). Here, since the input polarization state for each wavelength channel was different, the control powers applied to the thermal phase shifters depended on the wavelength channel, i.e., different tracks for the electric powers for each channel were obtained.

4. Discussion

This paper demonstrates a proof-of-concept automated adaptation and stabilization of an on-chip WDM PR, but it is necessary to mention the limitations of this two-channel design and suggest several improvements that can be made for practical implementation. Firstly, this design is not an endless polarization control design that can conduct a phase reset without a transient response [19], [32]. Two additional active MZIs are needed to form an endless phase shift design, which is necessary to implement endless polarization adaptation and stabilization. Secondly, for multi-channel WDM applications, the two-channel WDM PR needs to be extended for N-channel operation. For example, based on the two-channel scheme, an N-channel, tunable WDM PR can be realized by re-routing the waveguides with N tunable MZIs, 2$\times$N MRRs, and (N-1)$\times$N/2 optical crossings, see Fig. 8(a). Alternatively, to further reduce the footprint, we propose an improved N-channel, tunable WDM PR shown in Fig. 8(b). A waveguide loop is formed between two output ports of a PSR so that we can re-use MRR filters [11]. In this way, for each wavelength

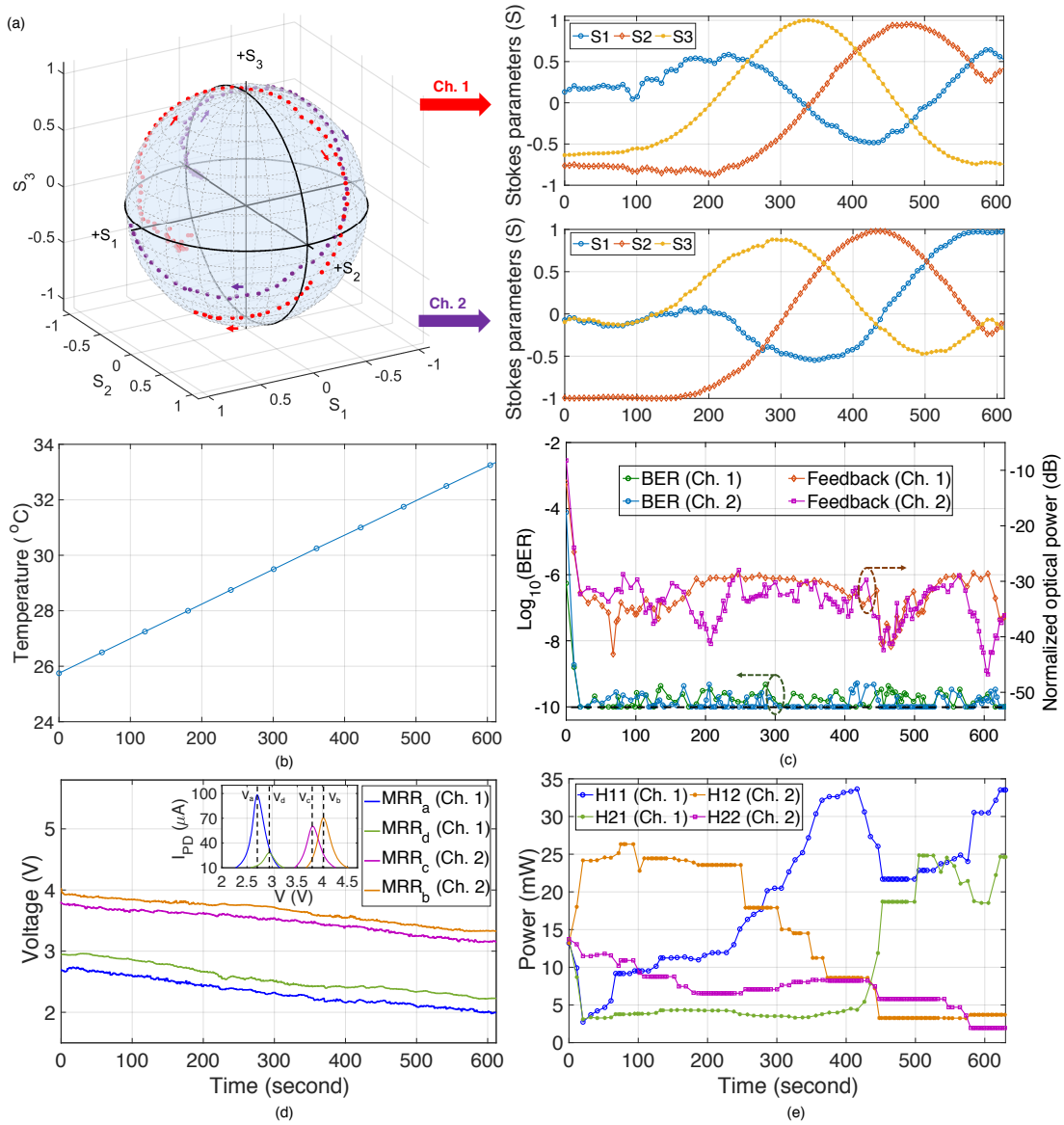

Fig. 7. Experimental results of the adaptation and stabilization of Ch. 1 and Ch. 2 for continuously changing input polarization states and chip temperatures: (a) The coordinates of the monitored polarization states on the Poincaré sphere and the corresponding normalized Stokes parameters versus tracking time; (b) Chip temperature versus tracking time; (c) BERs versus tracking time, a reference BER level (dash line), and normalized optical powers at feedback ports of the WDM PR versus tracking time; (d) Wavelength aligning and stabilization: applied voltages to the MRRs' IRPHs versus tracking time. Inset Figure: Initial IRPH's photocurrents (I_{PD}) measured while tuning the MRRs for the two channels; (e) Recorded applied electric power to the MZIs' thermal phase shifters versus tracking time.

This article has been accepted for publication in a future issue of this journal, but has not been fully edited. Content may change prior to final publication. Citation information: DOI 10.1109/JPHOT.2020.3012097, IEEE Photonics Journal

channel, the two outputs of the PSR are directed to the add-port and drop-port of a single MRR filter, respectively. This scheme simplifies the on-chip circuit design and significantly reduces the footprint and, therefore, the cost. More importantly, the automated adaptation and stabilization demonstrated in the paper can easily be adapted to such an N-channel WDM PR. The PSR used in our WDM PR can also be replaced by a more compact mode-evolution based PSR [33]. Thirdly, it should be noted that a time delay (the "TE-TM" delay) can result from the PSR and the differences between the "TE" and "TM" paths leading to the inputs to the tunable MZIs. However, in previous work [11], it has been shown that small "TE-TM" delays (less than 45 ps) do not detrimentally affect the data transmission. In other words, the receiver scheme can tolerate a significant amount of delay between the signals for the "TE" and "TM" polarizations before the BER starts to deteriorate. Here, it also should be pointed out that, due to its symmetric loop design, our improved, N-channel, WDM PR, shown in Fig. 8(b), will have less delay than the design presented in [11], even in the worst case. Nevertheless, it also has been proposed that implementing a variable optical delay line after one of the outputs of the PSR [14], [19], or that adjusting the waveguide length difference between the two paths, can be used to compensate for such signal delays. In addition, the improved N-channel design can simplify the control of the IRPHs by ensuring indefinite locking, i.e., it can circumvent the "halt" action as the same MRR is used to combine the data carried by the same wavelength on both polarization states, thus ensuring a maximum photocurrent at all times.

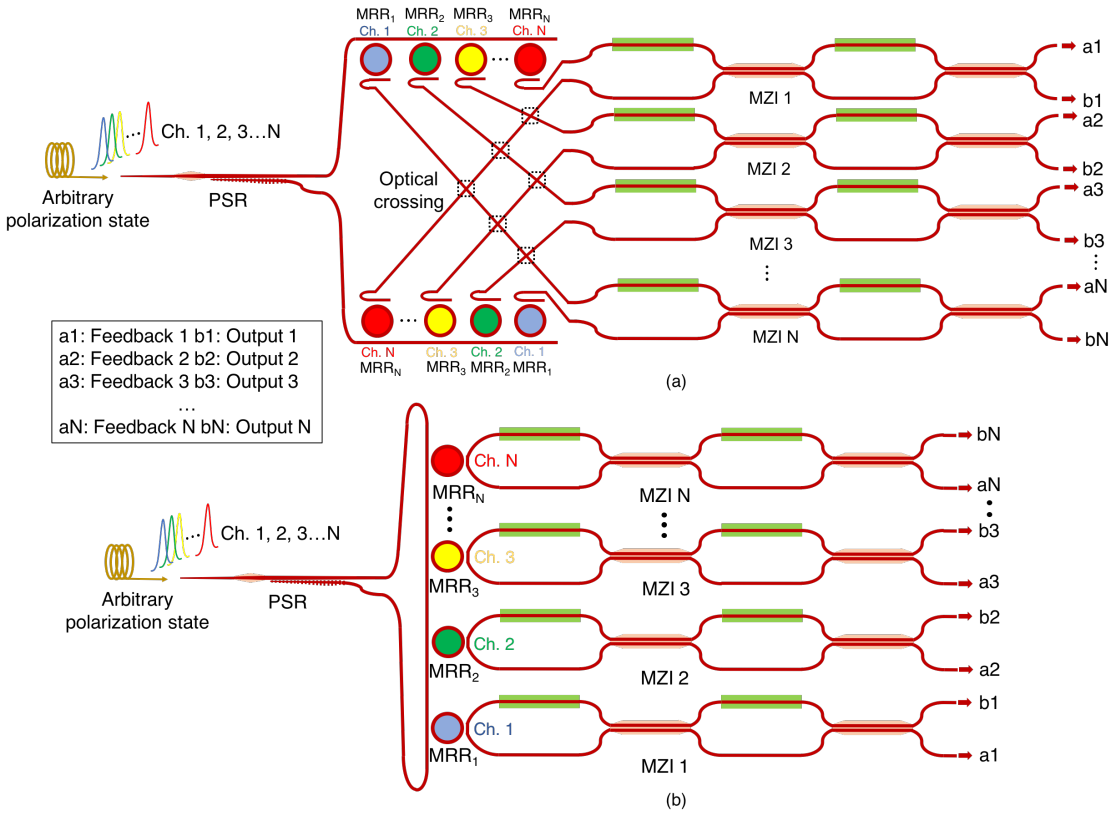

Fig. 8. Schematic of (a) an expanded N-channel WDM PR and (b) a proposed improved N-channel design. The single ring can be replaced with a double ring filter to improve the channel isolation [34], [35].

It is worth mentioning that when conducting our experiments, the response time was limited by the communications between the bench-top equipment used for control and data acquisition.

This article has been accepted for publication in a future issue of this journal, but has not been fully edited. Content may change prior to final publication. Citation information: DOI 10.1109/JPHOT.2020.3012097, IEEE Photonics Journal

However, in practice, the demonstrated active approach should be able to track polarization changes on the order of 10s to 100s of kHz. Since the IRPHs photo-detection response time is around 280 ns, and the IRPHs heating response time is around 900 ns [24], this speed is mainly limited by the TiN heater's response time (on the order of 10s of µs).

5. Conclusion

We have experimentally demonstrated automated adaptation and stabilization for a two-channel, tunable WDM polarization-independent receiver. Using a control algorithm based on Barzilai and Borwein's two-point step size gradient descent method, we realized automated wavelength tuning and stabilization, and automated polarization adaptation simultaneously for two wavelength channels, each having an arbitrary input polarization state. High-speed data was generated to modulate the optical input signals. Furthermore, we have implemented a long-duration, polarization and temperature varying experiment. The results present continuous polarization adaptation and stabilization for arbitrary input polarizations from standard optical fibers, and continuous stabilization of the desired wavelength channels for on-chip temperature changes. In addition, we have proposed an improved N-channel, tunable WDM polarization-independent receiver for practical WDM polarization applications. Our work paves the way toward developing fully automated, monolithic, data processing systems for multiple channels simultaneously, such as large-scale optical switches and coherent receivers.

Acknowledgment

We acknowledge CMC Microsystems for the design software and for providing access to the fabrication. We also thank the machine shop in the Department of Electrical and Computer Engineering at the University of British Columbia for assistance with regard to chip packaging.

References

[1] A. H. Ahmed, A. Sharkia, B. Casper, S. Mirabbasi, and S. Shekhar, "Silicon-photonics microring links for datacenters—challenges and opportunities," *IEEE J. Sel. Top. Quantum Electron.*, vol. 22, no. 6, pp. 194–203, 2016.

[2] A. N. Tait, H. Jayatilleka, T. F. De Lima, P. Y. Ma, M. A. Nahmias, B. J. Shastri, S. Shekhar, L. Chrostowski, and P. R. Prucnal, "Feedback control for microring weight banks," *Opt. Express*, vol. 26, no. 20, pp. 26 422–26 443, 2018.

[3] T. Barwicz, M. R. Watts, M. A. Popović, P. T. Rakich, L. Socci, F. X. Kärtner, E. P. Ippen, and H. I. Smith, "Polarization-transparent microphotonic devices in the strong confinement limit," *Nat. Photonics*, vol. 1, no. 1, p. 57, 2007.

[4] L. Chrostowski and M. Hochberg, *Silicon photonics design: from devices to systems*. Cambridge University, 2015.

[5] P. Dong, "Silicon photonic integrated circuits for wavelength-division multiplexing applications," *IEEE J. Sel. Top. Quantum Electron.*, vol. 22, no. 6, pp. 370–378, 2016.

[6] P. Dong, Y.-K. Chen, and L. L. Buhl, "Reconfigurable four-channel polarization diversity silicon photonic WDM receiver," in *Proc. Opt. Fiber Commun. Conf. Exhib. (OFC)*. Optical Society of America, 2015, pp. W3A–2.

[7] D. Y. Lee, X. Zheng, J. Yao, Y. Luo, J.-H. Lee, S. Lin, H. Thacker, J. Bovington, I. Shubin, S. S. Djordjevic, J. E. Cunningham, K. Raj, and A. V. Krishnamoorthy, "Error-free operation of a polarization-insensitive $4\lambda \times 25$ Gbps silicon photonic WDM receiver with closed-loop thermal stabilization of Si microrings," *Opt. Express*, vol. 24, no. 12, pp. 13 204–13 209, 2016.

[8] Y. Ma, Y. Liu, H. Guan, A. Gazman, Q. Li, R. Ding, Y. Li, K. Bergman, T. Baehr-Jones, and M. Hochberg, "Symmetrical polarization splitter/rotator design and application in a polarization insensitive WDM receiver," *Opt. Express*, vol. 23, no. 12, pp. 16 052–16 062, 2015.

[9] R. Gatdula, K. Kim, A. Melikyan, Y.-K. Chen, and P. Dong, "Simultaneous four-channel thermal adaptation of polarization insensitive silicon photonics WDM receiver," *Opt. Express*, vol. 25, no. 22, pp. 27 119–27 126, 2017.

[10] Y. Tan, H. Wu, and D. Dai, "Silicon-based hybrid (de) multiplexer for wavelength-/polarization-division-multiplexing," *J. Lightwave Technol.*, vol. 36, no. 11, pp. 2051–2058, 2018.

[11] A. H. K. Park, H. Shoman, M. Ma, S. Shekhar, and L. Chrostowski, "Ring resonator based polarization diversity WDM receiver," *Opt. Express*, vol. 27, no. 5, pp. 6147–6157, 2019.

[12] P. De Heyn, J. De Coster, P. Verheyen, G. Lepage, M. Pantouvaki, P. Absil, W. Bogaerts, D. Van Thourhout, and J. Van Campenhout, "Polarization-insensitive 5×20Gb/s WDM Ge receiver using compact Si ring filters with collective thermal tuning," in *Proc. Opt. Fiber Commun. Conf. Exhib. (OFC)*. Optical Society of America, 2014, pp. Th4C–5.

[13] L. Chen, C. R. Doerr, and Y.-k. Chen, "Polarization-diversified DWDM receiver on silicon free of polarization-dependent wavelength shift," in *Proc. Opt. Fiber Commun. Conf. Exhib. (OFC)*. IEEE, 2012, pp. 1–3.

[14] W. D. Sacher, T. Barwicz, B. J. Taylor, and J. K. Poon, "Polarization rotator-splitters in standard active silicon photonics platforms," *Opt. Express*, vol. 22, no. 4, pp. 3777–3786, 2014.

[15] P. Velha, V. Sorianello, M. Preite, G. De Angelis, T. Cassese, A. Bianchi, F. Testa, and M. Romagnoli, "Wide-band polarization controller for Si photonic integrated circuits," *Opt. Lett.*, vol. 41, no. 24, pp. 5656–5659, 2016.
[16] M. Ma, K. Murray, M. Ye, S. Lin, Y. Wang, Z. Lu, H. Yun, R. Hu, N. A. F. Jaeger, and L. Chrostowski, "Silicon photonic polarization receiver with automated stabilization for arbitrary input polarizations," in *Proc. Conf. on Lasers Electro-Opt. (CLEO): Science and Innovations*. Optical Society of America, 2016, pp. STu4G–8.
[17] H. Zhou, Y. Zhao, Y. Wei, F. Li, J. Dong, and X. Zhang, "All-in-one silicon photonic polarization processor," *Nanophotonics*, vol. 8, no. 12, pp. 2257–2267, 2019.
[18] M. Ma, H. Shoman, K. Tang, S. Shekhar, N. A. F. Jaeger, and L. Chrostowski, "Automated control algorithms for silicon photonic polarization receiver," *Opt. Express*, vol. 28, no. 2, pp. 1885–1896, 2020.
[19] C. R. Doerr, N. K. Fontaine, and L. L. Buhl, "PDM-DQPSK silicon receiver with integrated monitor and minimum number of controls," *IEEE Photonics Technol. Lett.*, vol. 24, no. 8, pp. 697–699, 2012.
[20] A. Melikyan, K. Kim, N. Fontaine, S. Chandrasekhar, Y.-K. Chen, and P. Dong, "Inter-polarization mixers for coherent detection of optical signals," *Opt. Express*, vol. 26, no. 14, pp. 18 523–18 531, 2018.
[21] D. A. B. Miller, "Self-configuring universal linear optical component," *Photonics Res.*, vol. 1, no. 1, pp. 1–15, 2013.
[22] C. Doerr, L. Chen, T. Nielsen, R. Aroca, L. Chen, M. Banaee, S. Azemati, G. McBrien, S. Park, J. Geyer *et al.*, "O, E, S, C, and L band silicon photonics coherent modulator/receiver," in *Proc. Opt. Fiber Commun. Conf. Exhib. (OFC)*. IEEE, 2016, pp. 1–3.
[23] A. H. Ahmed, D. Lim, A. Elmoznine, Y. Ma, T. Huynh, C. Williams, L. Vera, Y. Liu, R. Shi, M. Streshinsky, A. Novack, R. Ding, R. Younce, J. Roman, M. Hochberg, S. Shekhar, and A. Rylyakov, "A 6V Swing 3.6% THD$>$40GHz Driver with 4.5$\times$Bandwidth Extension for a 272Gb/s Dual-Polarization 16-QAM Silicon Photonic Transmitter," in *2019 IEEE International Solid-State Circuits Conf.-(ISSCC)*. IEEE, 2019, pp. 484–486.
[24] H. Jayatilleka, H. Shoman, L. Chrostowski, and S. Shekhar, "Photoconductive heaters enable control of large-scale silicon photonic ring resonator circuits," *Optica*, vol. 6, no. 1, pp. 84–91, 2019.
[25] K. Suzuki, R. Konoike, S. Suda, H. Matsuura, S. Namiki, H. Kawashima, and K. Ikeda, "Low-loss, low-crosstalk, and large-scale optical switch based on silicon photonics," *J. Lightwave Technol.*, 2019.
[26] T. Kurosu, T. Inoue, K. Suzuki, S. Suda, and S. Namiki, "High-capacity multi-stage operation of polarization-diversity silicon photonics 8$\times$ 8 optical switch," *J. Lightwave Technol.*, vol. 37, no. 1, pp. 131–137, 2019.
[27] H. Jayatilleka, K. Murray, M. Á. Guillén-Torres, M. Caverley, R. Hu, N. A. F. Jaeger, L. Chrostowski, and S. Shekhar, "Wavelength tuning and stabilization of microring-based filters using silicon in-resonator photoconductive heaters," *Opt. Express*, vol. 23, no. 19, pp. 25 084–25 097, 2015.
[28] J. Barzilai and J. M. Borwein, "Two-point step size gradient methods," *IMA J. Numer. Anal.*, vol. 8, no. 1, pp. 141–148, 1988.
[29] P. Sanchis, P. Villalba, F. Cuesta, A. Håkansson, A. Griol, J. V. Galán, A. Brimont, and J. Martí, "Highly efficient crossing structure for silicon-on-insulator waveguides," *Opt. Lett.*, vol. 34, no. 18, pp. 2760–2762, 2009.
[30] H. Yun, W. Shi, Y. Wang, L. Chrostowski, and N. A. F. Jaeger, "2$\times$2 adiabatic 3-dB coupler on silicon-on-insulator rib waveguides," in *Photon. North*, vol. 8915. International Society for Optics and Photonics, 2013, p. 89150V.
[31] H. Shoman, H. Jayatilleka, A. H. Park, A. Mistry, N. A. F. Jaeger, S. Shekhar, and L. Chrostowski, "Compact wavelength-and bandwidth-tunable microring modulator," *Opt. Express*, vol. 27, no. 19, pp. 26 661–26 675, 2019.
[32] C. R. Doerr and L. Chen, "Monolithic PDM-DQPSK receiver in silicon," in *36th Eur. Conf. Opt. Commun.* IEEE, 2010, pp. 1–3.
[33] M. Ma, A. H. K. Park, Y. Wang, H. Shoman, F. Zhang, N. A. F. Jaeger, and L. Chrostowski, "Sub-wavelength grating-assisted polarization splitter-rotators for silicon-on-insulator platforms," *Opt. Express*, vol. 27, no. 13, pp. 17 581–17 591, 2019.
[34] H. Jayatilleka, K. Murray, M. Caverley, N. A. F. Jaeger, L. Chrostowski, and S. Shekhar, "Crosstalk in SOI microring resonator-based filters," *J. Lightwave Technol.*, vol. 34, no. 12, pp. 2886–2896, 2015.
[35] H. Jayatilleka, H. Shoman, R. Boeck, N. A. F. Jaeger, L. Chrostowski, and S. Shekhar, "Automatic configuration and wavelength locking of coupled silicon ring resonators," *J. Lightwave Technol.*, vol. 36, no. 2, pp. 210–218, 2017.